HOKKAIDO UNIVERSITY

Title	Effects of Scandium and Zirconium Addition on Recrystallization Behavior of Al-Mg-Si Alloy
Author(s)	Ikeda, Ken-ichi; Takashita, Takuya; Akiyoshi, Ryutaro et al.
Citation	MATERIALS TRANSACTIONS, 59(4), 590-597 https://doi.org/10.2320/matertrans.L-M2018802
Issue Date	2018-04-01
Doc URL	https://hdl.handle.net/2115/75337
Type	journal article
File Information	Effects of Scandium and Zirconium Addition on Recrystallization Behavior of Al-Mg-Si Alloy.pdf

Hokkaido University Collection of Scholarly and Academic Papers : HUSCAP

Materials Transactions, Vol. 59, No. 4 (2018) pp. 590 to 597
©2018 The Japan Institute of Light Metals

Effects of Scandium and Zirconium Addition on Recrystallization Behavior of Al–Mg–Si Alloy*1

Ken-ichi Ikeda[1,*2], Takuya Takashita[2,*3], Ryutaro Akiyoshi[3,*4], Satoshi Hata[4], Hideharu Nakashima[4], Kazuhiro Yamada[5] and Kenji Kaneko[5]

[1]*Division of Materials Science and Engineering, Faculty of Engineering, Hokkaido University, Sapporo 060-8628, Japan*
[2]*Graduate Student, Department of Molecular and Material Sciences, Interdisciplinary Graduate School of Engineering Sciences, Kyushu University, Kasuga 816-8580, Japan*
[3]*Department of Molecular and Material Sciences, Interdisciplinary Graduate School of Engineering Sciences, Kyushu University, Kasuga 816-8580, Japan*
[4]*Department of Advanced Materials Science and Engineering, Faculty of Engineering Sciences, Kyushu University, Kasuga 816-8580, Japan*
[5]*Department of Materials Science and Engineering, Faculty of Engineering, Kyushu University, Fukuoka 819-0395, Japan*

The effects of thermally stabilized particles on the recrystallization behavior of an Al–Mg–Si alloy were investigated to obtain the fundamental knowledge for controlling the microstructure, texture, and mechanical properties of this alloy. In this study, the Al–Mg–Si–Sc–Zr alloy was cast, homogenized, and hot-rolled. Three types of spherical $Al_3(Sc, Zr)$ particles with $L1_2$ structure, rod-like incoherent, spherical semi-coherent, and spherical incoherent particles, were observed in a hot-rolled sample of the Al–Mg–Si–Sc–Zr alloy using transmission electron microscopy (TEM), scanning transmission electron microscopy (STEM), and energy-dispersive X-ray spectroscopy (EDS). In addition, three-dimensional electron tomography (3D-ET) and STEM-EDS revealed that all particles have a core-shell structure with a Sc-enriched core and a Zr-enriched shell. It is considered that these particles are formed during casting, homogenized treatment, and hot rolling. The crystal orientation distribution of the sample after cold rolling indicated that the presence of $Al_3(Sc, Zr)$ particles may interfere with the recrystallization (grain growth) until 600°C. Comparison with the driving force of primary recrystallization and grain growth, and the pinning force of $Al_3(Sc, Zr)$ particles, showed that these particles mainly contribute to the suppression of grain growth. The results of an in-situ heating SEM/EBSD analysis of the cold-rolled Al–Mg–Si–Sc–Zr alloy supported this suggestion. [doi:10.2320/matertrans.L-M2018802]

(Received November 29, 2017; Accepted January 4, 2018; Published March 25, 2018)

Keywords: *Al–Mg–Si alloy, recrystallization, precipitation, grain growth, pinning force*

1. Introduction

Application of aluminum alloys in automotive structural materials have been increased in recent years for reducing vehicle body weight. Balancing between the formability and the strength is very important for automotive sheet materials. Al–Mg–Si alloys can be strengthened further by a press forming process in an annealed material, and by subsequent paint baking for forming β'' phase. Consequently, it can be described that Al–Mg–Si alloys are the most suitable aluminum alloys for automotive sheet materials.[1)] However, the strength of such alloys is still inferior to that of steel plates in the 340-MPa or the 440-MPa classes.[2)] Therefore, if an Al–Mg–Si alloy with the right balance between good ductility and high strength could be developed without impairing its press formability, that would lead to further expansion of its demand.

In general, the material strengthening methods include solid solution, precipitation, and grain refinement strengthening. In particular, in the case of precipitation strengthening, high strength can be achieved by the formation of thermally stable precipitates which suppress the grain coarsening resulting that of fine grains. Al–Zn–Mg alloys are known as the precipitation-strengthened alloys with poor ductility, unsuitable for the press-forming processes. Therefore, it is necessary to design a material based on the Al–Mg–Si alloys, with precipitation of thermally stable particles.

In this study, we selected scandium (Sc) and zirconium (Zr), which form intermetallic compounds with aluminum. Sc and Zr added aluminum alloys have been attracted a large attention and studied intensively because they exhibit excellent mechanical properties. According to the Al–Sc–Zr ternary phase diagram at 500°C and 600°C, it has been reported that there is a large region where Al_3Sc, Al_3Zr and α-Al matrix are in an equilibrium.[3)] In this region, Al_3Sc and Al_3Zr form a composite phase known as $Al_3(Sc, Zr)$,[3)] known to be more stable in terms of its energy, thermal, and electronic structure than that of Al_3Sc. In addition, $Al_3(Sc, Zr)$ has a slow coarsening rate at high temperatures and it is known to be a very stable phase.[4)] The morphology of $Al_3(Sc, Zr)$ precipitates in an Al–Sc–Zr alloy is spherical, and it forms a core-shell structure with high Sc concentration at its core part and high Zr concentration at its shell part.[5)] It has been reported that the reason behind this is the difference in diffusion rate; Sc in aluminum has a much faster diffusion rate than that of Zr; thus, precipitation occurs in such a way that Al_3Zr coats the Al_3Sc after its precipitation. Furthermore, in a study of Al–Sc alloys, it has been shown that a supersaturated solid solution containing Sc is thermally unstable, and its decomposition rate is remarkably fast.[4)] Therefore, Al_3Sc precipitates uniformly in the matrix within a short period of time, and subsequently, $Al_3(Sc, Zr)$ also precipitates uniformly, as well. The crystal structure of

*1This Paper was Originally Published in Japanese in J. JILM **66** (2016) 609–616.
*2Corresponding author, E-mail: ikeda.ken-ichi@eng.hokudai.ac.jp
*3Graduate Student, Kyushu University. Present address: JFE Steel Corporation, Chiba 260-0835, Japan
*4Graduate Student, Kyushu University. Present address: Kobe Steel, Ltd., Moka 321-4367, Japan

Al_3(Sc, Zr) has $L1_2$ structure, and its lattice misfit with the aluminum matrix is as low as about +1.3%. The interface energy between Al_3(Sc, Zr) and the matrix is low, which results coherent precipitates. Moreover, when crystallization occurs during the solidification, it is thought that it acts as a nucleation site for effective recrystallized grains.

Al_3(Sc, Zr) precipitates uniformly in the matrix, highly coherent with the matrix, and has high thermal stability. These three characteristics leads us to expect that the strength can be improved greatly by the precipitation strengthening and the grain refinement strengthening. Because the grain refinement strengthening has less ductility deterioration than other strengthening methods. It is thought that the Al_3(Sc, Zr) precipitates will lead to increase the strength maintaining the ductility.

Detailed studies[5–9] on the aging behavior from a supersaturated solid solution have been carried out with Al–Sc–Zr ternary alloys. On one hand, the results show the excellent characteristics of Al_3(Sc, Zr), i.e. high temperature for a long period is required to decompose it into a supersaturated solid solution, because it has high thermal stability. For example, in the study by Iwamura *et al.*,[5] they have applied solution treatment at 650°C for 200 h, to decompose Al_3(Sc, Zr). However, such heat treatment is impractical in the real production process. Therefore, we used the alloy which contains second phase particles from the beginning and focused on the acquirement of fundamental knowledge of recrystallization behavior.

In this study, we fabricated a Sc and Zr-added Al–Mg–Si alloy and investigated the grain growth behavior of recrystallized grain during the heat treatment process. We investigated the feasibility of the Sc and Zr-added Al–Mg–Si alloy as a potential material for practical applications.

2. Experimental Procedure

In this study, Sc and Zr were added to Al–Mg–Si alloy with its final composition as Al–0.5Mg–0.5Si–0.3Sc–0.2Zr (the numerical values represent mass%), hereinafter referred to as "Alloy A." Additionally, an Al–0.5Mg–0.5Si alloy, hereinafter referred to as "Alloy B," was used for comparison. Both alloys were subjected to homogenized treatment (550°C for 4 h) and hot rolling (with the rolling start temperature at 400°C, rolling reduction of 78%, and 10 mm thickness). Microstructural studies were carried out on the hot-rolled samples by transmission electron microscope (TEM) and scanning transmission electron microscope (STEM) to observe the distribution and composition of the second phase particles, and compositional analyses by STEM-energy dispersive X-ray spectroscopy (EDS). In addition, three-dimensional electron tomography (3D-ET) method was also carried out to understand the morphology of the second phase particles. For the 3D-ET observation, HATA-8075 manufactured by Mel-Build Co. was used as a sample holder, and tilt-series STEM images were acquired at a tilt range of ±75° with 1° to 2° step; then, three-dimensional reconstructions were performed by the sequential iterative reconstruction technique (SIRT).

To evaluate the recrystallization behavior during the thermo-mechanical treatment, the hot-rolled samples were cold-rolled with a rolling reduction of 90%. The cold-rolled samples were annealed at three different temperatures, 400°C, 500°C, and 600°C for 1 h after cold rolling, and their cross-section in the rolling direction (RD plane) were analyzed using the scanning electron microscope/electron back scattered diffraction (SEM/EBSD) method. TEM/STEM observation and structural evaluation by the 3D-ET method were also performed to study the distribution of particles. Furthermore, an *in-situ* heating SEM/EBSD analysis using a heating stage for SEM was carried out in 50°C increments from 300°C to 450°C to study the structural change during the heat treatments. The holding time at each temperature was 1.5 h, and the analyzed surface was the rolled surface (ND plane). The observation sample preparation method for the SEM/EBSD method was the same method as that we reported for Al–Mg–Si alloy.[10] The influence of the addition of Sc and Zr is investigated from the microstructural information of Alloy A, in particular the presences of the second-phase particles, and recrystallization behavior from the cold-rolled-annealed samples. Figure 1 shows the flow of the sample production process and experiment.

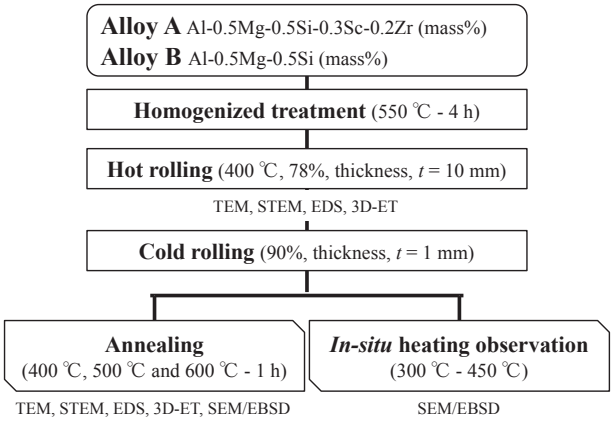


Fig. 1 Production and experimental process of samples.

3. Results and Discussion

3.1 Microstructural analysis of hot-rolled samples

The observation from the cross section in the vertical direction of ND and RD (TD plane) of the hot-rolled sample of Alloy A and Alloy B revealed that the grain width of Alloy A was 6 to 18 μm and that of Alloy B was 65 to 300 μm. These results showed that the grains were refined at the hot rolling by co-adding of Sc and Zr. It is believed that Al_3(Sc, Zr) crystallized during the solidification in the casting of Alloy A, and the grains became finer. Figure 2 shows the high-angle annular dark-field (HAADF)-STEM image of the hot-rolled samples of both alloys. The region shown with a bright contrast in the HAADF-STEM image indicates that an element with a large atomic number exists, revealing that the Alloy A contains second phase particles in various morphology, such as spherical and rod shapes. As a result of determining the aspect ratio of the second phase particles from the HAADF-STEM image in Fig. 2(a), it was found that the aspect ratio of the spherical particles was 1.5 or less and of rod-like particles was 1.5 or more, they were mixed

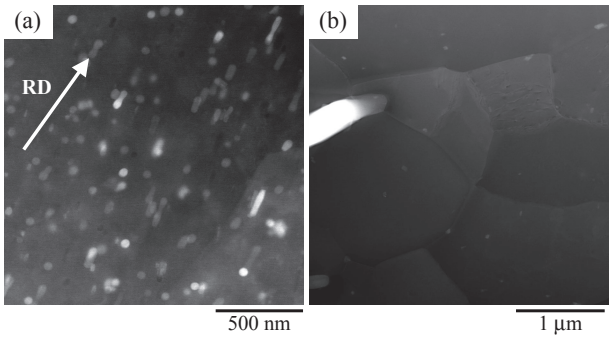


Fig. 2 HAADF-STEM images of hot-rolled sheets: (a) Al–Mg–Si–Sc–Zr (Alloy A) and (b) Al–Mg–Si (Alloy B).

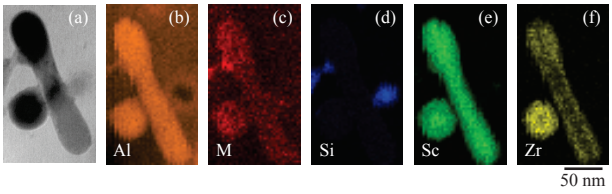


Fig. 3 (a) HAADF-STEM image and (b)–(f) STEM-EDS elemental maps of particles in hot-rolled sheet of Alloy A.

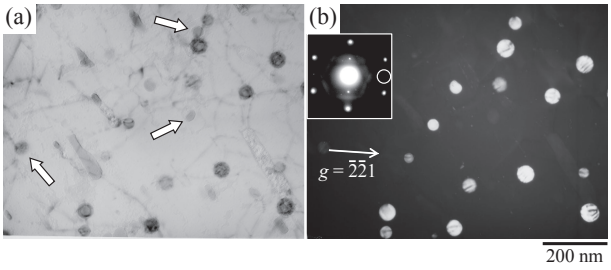


Fig. 4 (a) BF-TEM image and (b) DF-TEM image of particles in hot-rolled sheets of Alloy A.

together, and the longitudinal axis of the rod-like particles was oriented in the rolling direction. The main components of the spherical particle were found as Al, Sc, and Zr, and those of the rod-like particle as Al and Si or Al, Sc, and Zr from EDS point analysis of particles. Because this alloy is classified as an excess Si alloy in Al–Mg–Si alloys, it is expected that Si would crystallize or precipitate individually. Therefore, it is feasible that the two types of particles with different compositions could be present in the rod-like particles. Figure 3 shows the STEM-EDS elemental distribution maps of spherical particles and those of rod-like particles, where Al, Sc, and Zr were present in the Alloy A. Elemental distribution maps of Sc and Zr confirms that the core-shell structure of $Al_3(Sc, Zr)$ precipitates is formed as has been reported.[5] Figure 4(a) shows the TEM bright-field image in the region where spherical and rod-like particles were observed within the same grain. Further, Fig. 4(b) displays an electron diffraction pattern of the electron incident beam direction ⟨114⟩, which shows an ordered lattice reflection caused by the $L1_2$ structure. The white circle shows the TEM dark field image formed by the diffraction beam of the ordered lattice reflection shown in Fig. 4(b). As most of the spherical particles which present in the bright field image are shown in the dark field image, it is suggested that $Al_3(Sc, Zr)$ precipitated with a specific orientation relationship with the matrix. Furthermore, the bright field images under two beam conditions using $2\bar{2}0$ diffraction beams showed wavelike Moiré fringe in these spherical particles. In the case of coherent particles, a coffee bean-shaped strain contrast, the Ashby-Brown contrast, is observed at the particles, but it changes to wavelike contrast as it becomes incoherent.[11] Therefore, it was revealed that the spherical particles observed in Fig. 4(b) are probably incoherent particles. On the other hand, the spherical and rod-like particles indicated by white arrows in Fig. 4(a) were not observed in the dark-field image, Fig. 4(b). In order to confirm whether the rod-like particles were $Al_3(Sc, Zr)$ having the $L1_2$ structure or not, the extractive replica sample for TEM was observed, and an electron diffraction pattern of only precipitates was analyzed. The result confirmed that the rod-like particles were $Al_3(Sc, Zr)$ with the $L1_2$ structure. The only difference from the spherical particles observed in Fig. 4(b) and the rod-like particles was that the spherical particles did not have an orientation relationship with the matrix. If we take into account the Al–Sc–Zr ternary alloy casting reported by Norman *et al.* and the results of the studies of hot-rolled 5754 aluminum alloys with co-added Sc and Zr as reported by Fuller *et al.*,[12,13] it could be considered that the rod-like particles were generated by eutectic reaction during solidification after casting. In the case of the spherical particles (white arrows) that were not observed in Fig. 4(b), from the STEM-EDS it was found that the Sc concentrated region was present in the spherical particle. Furthermore, when the STEM-EDS and 3D-ET were combined and subjected to the elemental analysis, it was confirmed that the Sc-enriched region was present in a cylindrical shape.[14] It is considered that the rod-like particles were separated during hot rolling and spheroidized processes.

Based on these results, it was revealed that $Al_3(Sc, Zr)$ with $L1_2$ structure would become available when a small amount of Sc and Zr was added to the Al–Mg–Si alloy. In the hot-rolled samples, two types of spherical particles with and without orientation relationship and rod-like particles coexist. The spherical particles with and without an orientation relationship with the matrix suggest that they were formed during the homogenization treatment and the solidification, respectively.

3.2 Microstructure analysis of cold-rolled and annealed samples

Figure 5 shows the crystal orientation distribution of the RD plane after the cold rolling of each alloy. The color shows the orientation of the ND plane of each crystal (hereinafter, the crystal orientation distribution maps show the same ND plane orientation distribution). Alloy A has a narrower grain size distribution than Alloy B. As stated in Section 3.1, the grain size distribution width has become narrower when $Al_3(Sc, Zr)$ is introduced in Alloy A after hot-rolling, and it probably remained its influence on the grain size, even after cold-rolling. Both alloys were occupied by brass, copper, and S orientations, which are the typical rolling textures of the aluminum alloy; besides, there were no major differences in the texture.

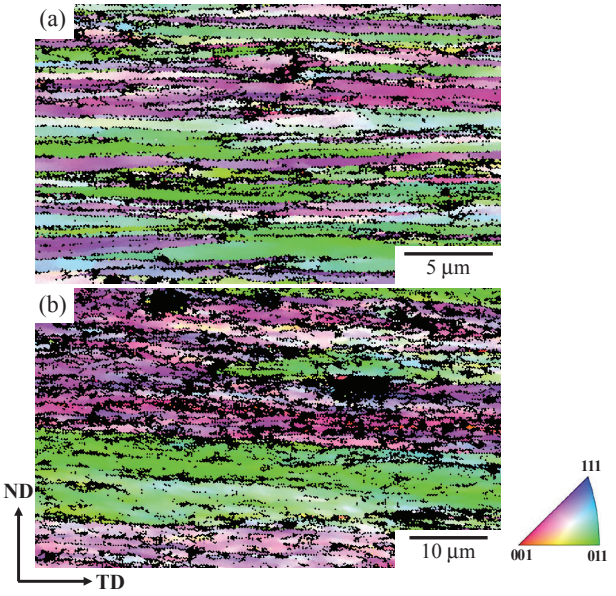


Fig. 5 ND plane crystal orientation distribution maps of cold-rolled sheets: (a) Alloy A and (b) Alloy B.

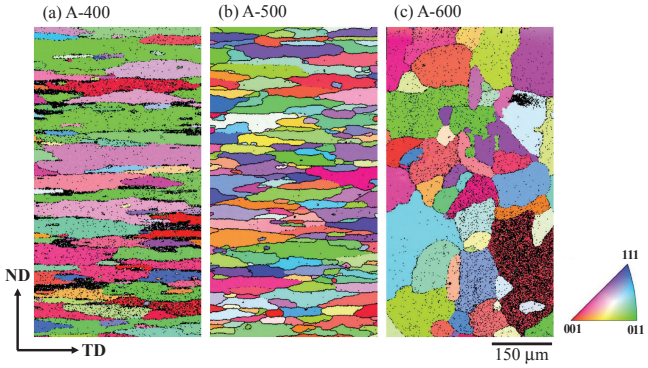


Fig. 6 ND plane crystal orientation distribution maps of cold-rolled and annealed sheets of Alloy A: (a) A-400, (b) A-500 and (c) A-600.

Figure 6 shows the crystal orientation distribution map on the RD plane after annealing of the cold-rolled samples of Alloy A at 400°C (A-400), 500°C (A-500), and 600°C (A-600) for 1 h. Elongated grains are found in A-400 and A-500, and the influence of cold rolling remained. However, it was found that the elongated grains were grown along the ND direction with A-600. Figure 7 shows the crystal orientation distribution on the RD plane of Alloy B after each heat treatment (named as B-400, B-500, and B-600). With B-400, the influence of cold rolling remained as occurrences of elongated grains, nevertheless grains were grown in an equiaxial manner with B-500 and B-600.

According to the crystal orientation relationship shown in Fig. 6 and Fig. 7, the distribution of the texture component was confirmed. Although Alloy A had a random crystal orientation distribution, a recrystallized texture with highly cube-oriented grains was formed in the annealed Alloy B. $Al_3(Sc, Zr)$ particles therefore cause a different recrystallized grain growth in Al–Mg–Si alloy during the annealing after cold rolling. Moreover, because texture is randomized due to $Al_3(Sc, Zr)$ particles, a structural control may take place and contributes to improvements in the formability.

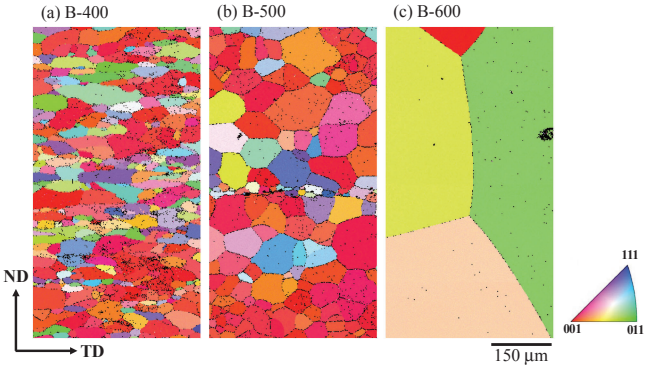


Fig. 7 ND plane crystal orientation distribution maps of cold-rolled and annealed sheets of Alloy B: (a) B-400, (b) B-500 and (c) B-600.

3.3 Influence of $Al_3(Sc, Zr)$ particles on recrystallized grain growth

As shown in 3.2, it was shown that the Al–Mg–Si alloy changes its microstructural formation process during the thermo-mechanical treatment by the presence of $Al_3(Sc, Zr)$ particles. A quantitative evaluation on how $Al_3(Sc, Zr)$ affects the formation process of Al–Mg–Si alloy was conducted based on the microstructural observation. The deformed structure changed to stable structure by the annealing after cold-rolling, through a recovery, primary recrystallization, and normal grain growth, or secondary recrystallization. During each process, the progress or delay of recrystallization was determined by the correlation between the driving force of recrystallization and the Zener force (grain boundary pinning force) of the particles. In other words, if the driving force is larger than the Zener force, then the recrystallization proceeds, and *vice versa*. In this study, the driving force of recrystallization was determined by the SEM/EBSD method from the crystal orientation. The Zener force of $Al_3(Sc, Zr)$ particles was derived from the spatial distribution information obtained by TEM/STEM observation and the 3D-ET method.

3.3.1 The driving force of primary recrystallization of cold-rolled samples

The recrystallization during the annealing of cold worked metals is called primary recrystallization, and the driving force of it is the stored strain energy introduced by the process. The dislocation substructures introduced during the cold working is recovered in the early stages of annealing. In other words, there are many sub-grains within the grains.

In this study, the driving force was evaluated by the results obtained by the SEM/EBSD method of sub-boundary energy from the cold-rolled samples, as the stored strain energy.[15] Based on the orientation information of the cold-rolled sample of Alloy A, as shown in Fig. 5, we observed the boundary where the orientation difference between the measured neighboring grains less than 15°, as a sub-boundary perpendicular to the observation plane, and the grain boundary energy γ_i at misorientation θ_i was calculated by the Read-Shockley's Equation,[16,17] eq. (1).

$$\gamma_i = \gamma_m \frac{\theta_i}{\theta_m}\left(1 - \ln\frac{\theta_i}{\theta_m}\right) \quad (1)$$

where, γ_m and θ_m are the energy and the misorientation of high angle grain boundary, 0.32 J/m^2 and 15°,[18] respectively.

The crystal orientation distribution map using regular hexagonal pixels were created by the SEM/EBSD method. The boundary length between the measuring points becomes $x/\sqrt{3}$, when the distance between the measuring points, x, is chosen. It is possible to obtain the sub-boundary energy per unit length using the formula $n_i \cdot \gamma_i \cdot x/\sqrt{3}$, with this boundary length as a unit length and the number of sub-boundaries n_i and a misorientation θ_m within the observation region. The total sum of the sub-boundary energy with less than 15° in the observation region γ_t will be $\gamma_t = \sum \gamma_i$. The driving force of the primary recrystallization can be measured by subtracting the γ_t from the observed region. The driving force P_I [J/m^3 = Pa] of the primary recrystallization can be measured from eq. (2),

$$P_I = \frac{\gamma_t}{S} \tag{2}$$

where S is the observed area. The values of γ_t and S, obtained from the sub-boundary length with misorientation less than 15° from the cold-rolled Alloy A sample is shown in Fig. 5(a), were 7.69×10^{-4} J/m and 6.49×10^{-10} m^2, respectively. When P_I was calculated in eq. (2), the driving force was 1.18 MPa. This value will be compared with the Zener force of particles and the driving force of normal grain growth, as discussed in 3.3.2.

3.3.2 Zener force of Al_3(Sc, Zr) particles

Dispersed particles, such as precipitates, contribute to the increase in strength by dispersion (precipitation) strengthening. Therefore, distribution of particles is also an important factor from the viewpoint of grain size and texture control. Because the elementary process of recrystallization is grain boundary migration, the dispersed particles in grains will inhibit grain boundary migration, leading to various phenomena, such as grain refinement. As shown in 3.1, a small amount of Sc and Zr in the Al–Mg–Si alloy induces many Al_3(Sc, Zr) particles, such as crystallized products and precipitates in the grains. In this section, we investigate the Zener force[18,19] of the particles in the annealed cold-rolled samples. The interaction between the particles and grain boundaries is greatly influenced by the coherency. Figure 8(a) is a schematic image showing the influence of the incoherent particle on the boundary migration. The boundary moves in the Y direction in this figure. The force acting in the direction opposite to the direction of grain boundary migration is the Zener force. From Fig. 8(a), it is possible to express the Zener force using the grain boundary energy, γ_{gb}, and particle diameter, d, and the Zener force per incoherent particle, F_i,

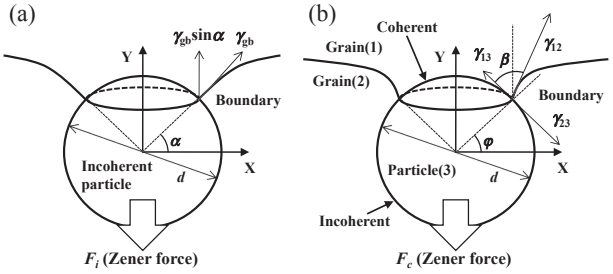


Fig. 8 The interaction between a grain boundary and a spherical particle: (a) an incoherent particle and (b) a coherent particle.

will be given by eq. (3),

$$F_i = \pi d \cos\alpha \cdot \gamma_{gb} \sin\alpha \tag{3}$$

where, α is the angle between the grain boundary and particles. When $\alpha = 45°$, the maximum value would be F_{is}, and the value would thus be

$$F_{is} = \frac{\pi d \gamma_{gb}}{2} \tag{4}$$

Based on this equation, the Zener force of incoherent particle, P_i, per unit volume will be calculated. When the number of incoherent particles per unit volume is designated as N_v the number of particles that the grain boundary contacts per unit area, N_s will be $N_s = d \cdot N_v$. When there is no size distribution in the particles, the Zener force, P_i, is given by eq. (5).

$$P_i = N_s \cdot F_{is} = \frac{N_v \pi d^2 \gamma_{gb}}{2} \tag{5}$$

Figure 8(b) is a schematic image showing the relationship between the coherent particle and the grain boundary migration. The direction of the grain boundary migration is the same as that of the incoherent particles. These particles have a coherent relationship to Grain (1) and an incoherent relationship to Grain (2). Considering the energy balance at the interface between the particle surface and grain boundaries, the following equation can be used:

$$\gamma_{23} = \gamma_{13} + \gamma_{12} \cos\beta \tag{6}$$

where, γ_{12} is the grain boundary energy, γ_{13} represents the energy between Grain (1) and the coherent interface energy of particle, γ_{23} is the energy between Grain (2) and the incoherent interface energy of particle, and β is the angle shown in Fig. 8(b). From this equation, the Zener force, F_c per coherent particle will be expressed as eq. (7):

$$F_c = \pi d \cos\varphi \cdot \gamma_{12} \cos(\beta - \varphi) \tag{7}$$

where φ is the angle between the grain boundary and the coherent particle. When $\varphi = \beta/2$ and $\beta = 0$, it will become the maximum value, F_{cs}, and that value will be:

$$F_{cs} = \pi d \gamma_{12} \tag{8}$$

The Zener force, P_c of the coherent particle per unit area of the grain boundary is given by eq. (9):

$$P_c = N_s \cdot F_{cs} = N_v \pi d^2 \gamma_{12} \tag{9}$$

When eqs. (5) and (9) are compared, and the angle between the grain boundary and particle is less than 90°, the Zener force of the coherent particles becomes larger.

In this study, particles in the annealed Alloy A samples at 500°C and 600°C (A-500, A-600) were observed to obtain their particle coherency, N_v and average particle diameter, d, using TEM/STEM and 3D-ET method. Figures 9(a)–(b) and (c)–(d) are HAADF-STEM images — the 3D reconstructed images of particles in the A-500 and A-600 samples, respectively. From analyzing d and N_v of both samples which were obtained based on spatial distribution information of multiple fields, it was found that $d = 45.7$ nm and $N_v = 1.15 \times 10^{20}$/m^3 for A-500, and $d = 89.9$ nm and $N_v = 3.25 \times 10^{19}$/m^3 for A-600. Moreover, it became clear that

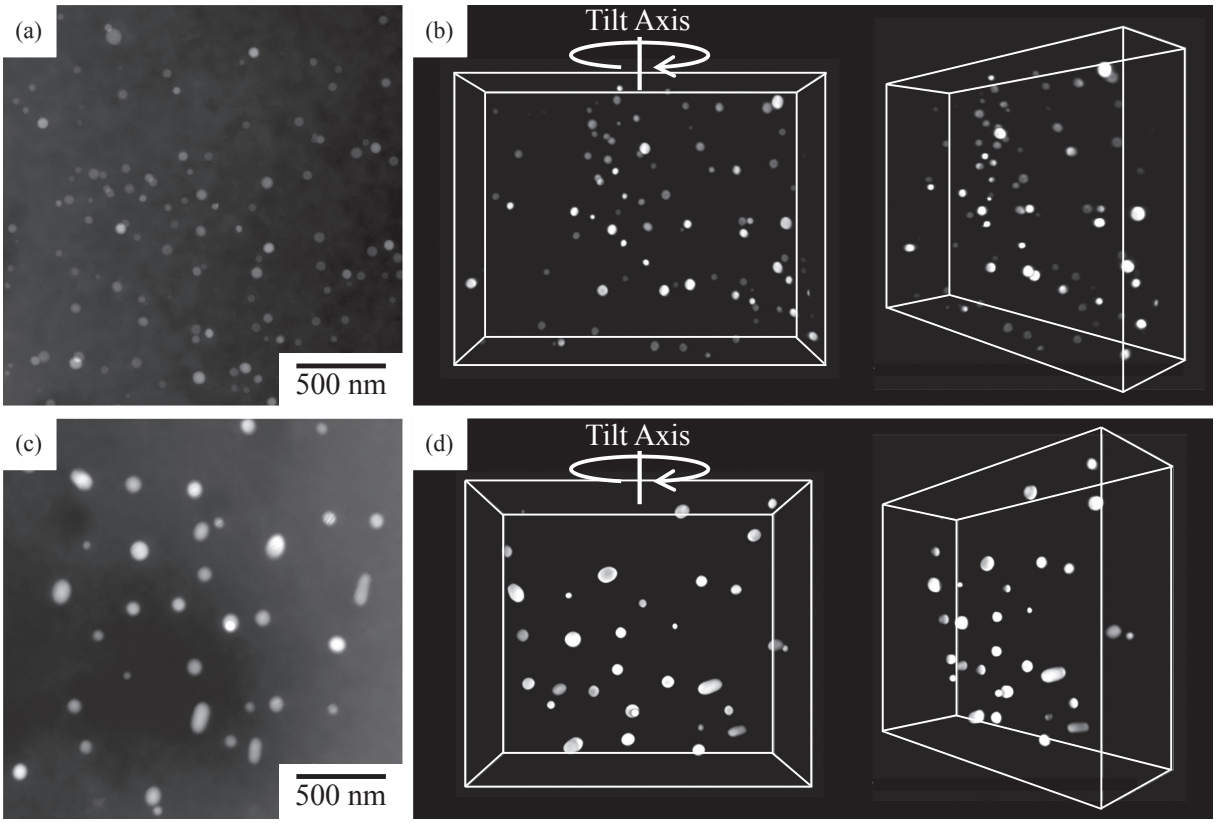


Fig. 9 HAADF-STEM images and 3D reconstructed view of Al_3(Sc, Zr) particles in (a), (b) A-500 and (c), (d) A-600.

the frequency of the presence of the rod-like particles was remarkably reduced. Therefore, it was considered that the rod-like particles can be ignored for calculation of the Zener force. Furthermore, evaluating the coherency of the spherical particles by TEM observation revealed that almost all particles in A-600 were found to be incoherent. It was found that semi-coherent particles and incoherent particles were mixed in A-500. It was obtained that the semi-coherent particles of A-500 had $d = 46.3$ nm, and $N_v = 3.10 \times 10^{19}/m^3$, and the incoherent particle had $d = 45.1$ nm and $N_v = 8.38 \times 10^{19}/m^3$. Therefore, to evaluate the Zener force of A-500, eq. (5) was used for the incoherent particles and eq. (9) was used for the semi-coherent particles. Furthermore, for the grain boundary energies, γ_{gb} and γ_{12} were regarded as the grain boundary energy of the high angle grain boundary; $0.32\,J/m^2$. As a result, the Zener force P_{z500} $(= P_i + P_c)$ of the A-500 sample was 0.16 MPa, and the Zener force of A-600, P_{z600} $(= P_i)$ was 0.13 MPa.

3.3.3 Driving force of grain growth during annealing

The grain growth occurs during annealing after primary recrystallization. In the grain growth process, the driving force is the force with which the curved grain boundary becomes flat, and it is dependent on the grain boundary energy. The driving force of the grain growth is expressed in eq. (10),[18)]

$$P_{II} = \frac{A\gamma_{gb}}{R} \tag{10}$$

where, R is the radius of curvature of the grain boundary and A is a constant. It can be seen from eq. (10) that as the grain size decreases, the driving force of the grain growth becomes larger. In this study, the maximum driving force of the grain growth was obtained from the minimum crystal grain size of samples. From the crystal orientation distribution of Fig. 6, the minimum crystal grain radii of A-500 and A-600 were 4.1 μm and 7.9 μm, respectively. When $A = 1$ and $\gamma_{gb} = 0.32\,J/m^2$ were used, the driving force of A-500 and A-600 were $P_{II500} = 0.078$ MPa, and $P_{II600} = 0.041$ MPa, respectively.

From these investigations, it was found that the driving force P_I $(= 1.18$ MPa) of the primary recrystallization is much larger than the Zener force. Namely, Al_3(Sc, Zr) spherical particles are not expected to be a strong hindrance for primary recrystallization in the annealing process of Alloy A at 500°C and at 600°C. On the other hand, the driving force of the grain growth after the primary recrystallization is smaller than the Zener force. Therefore, it is expected that the Al_3(Sc, Zr) spherical particles may be an obstacle to grain growth.

3.4 Evaluation of recrystallization behavior by *in-situ* heating SEM/EBSD analysis

As discussed in Section 3.3, it was suggested that the Al_3(Sc, Zr) spherical particles influence the subsequent grain growth behaviors rather than during the primary recrystallization. We will examine the prediction result by elucidating the recrystallization behavior by using *in-situ* heating SEM/EBSD analysis.

Figure 10 shows the results of cold-rolled sample of Alloy A. The black region in the figure is a region with poor analytical reliability owing to the presence of high strain regions and grain boundaries. The sample before the heat

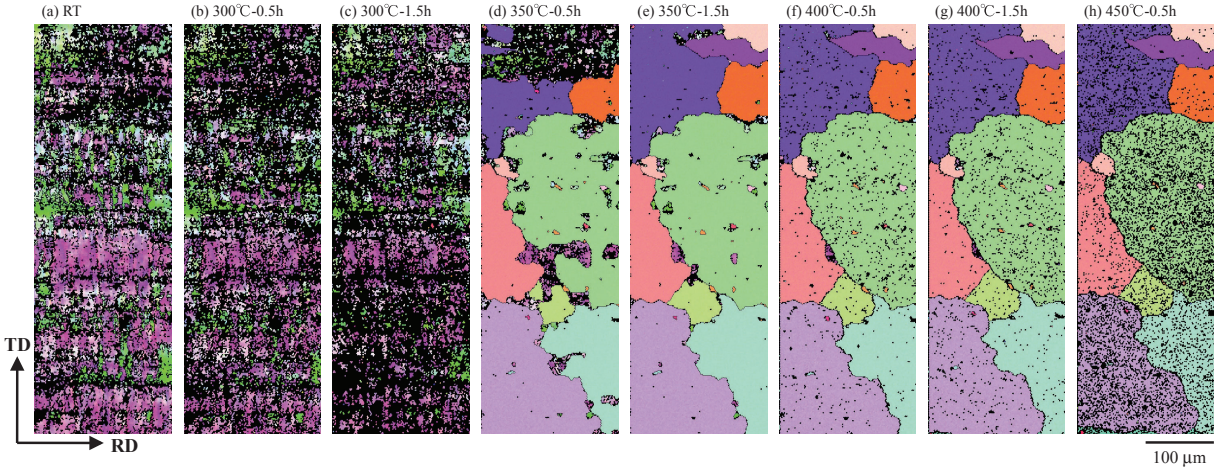


Fig. 10 ND plane crystal orientation distribution maps of cold-rolled sheet of Alloy A by using *in-situ* heating EBSD analysis.

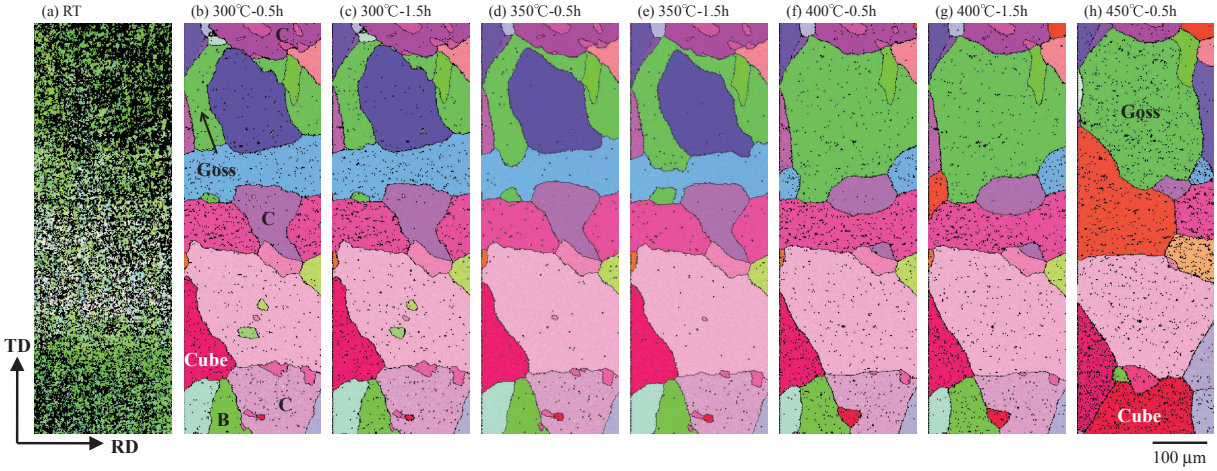


Fig. 11 ND plane crystal orientation distribution maps of cold-rolled sheet of Alloy B by using *in-situ* heating EBSD analysis.

treatment has a typical cold-rolled structure. After the heat treatment at 300°C, it had almost the same structure as the cold-rolled texture, and there were no significant changes. However, at 350°C, grain growth was observed. The cold-rolled texture in the field almost disappeared by the heat treatment at 350°C, but it is found that the subsequent grain growth did not occur in the heat treatment up to 450°C. Furthermore, the recrystallized grain boundary is curved in many parts, suggesting that the Al_3(Sc, Zr) particles had pinned the grain boundaries.

Figure 11 shows the results of cold-rolled sample of Alloy B. The sample before the heat treatment also had a cold-rolled structure like Alloy A, however it grew rapidly with heat treatment at 300°C, and the cold-rolled structure was consumed by this temperature. Moreover, during the heat treatment from 350°C to 450°C, the grain growth occurred continuously.

From the viewpoint of recrystallization texture components, it was found that the recrystallized grains of Alloy A didn't have these components, while those of Alloy B had many components. Namely, in Alloy B, the recrystallized grains with rolling texture components of brass orientation ($\{110\}\langle 112\rangle$: B) and copper orientation ($\{112\}\langle 111\rangle$: C) grew until 350°C, and the cube orientation ($\{100\}\langle 001\rangle$) and Goss orientation ($\{110\}\langle 001\rangle$) started growing by consuming the surrounding grains after 400°C.

From the above results, it was found that the presence of Al_3(Sc, Zr) particles significantly changes the recrystallization behavior of the Al–Mg–Si alloy, maintaining the grain shape after completion of the primary recrystallization, up to 450°C. The observation also revealed that the Al_3(Sc, Zr) particles not only caused the pinning of grain growth after primary recrystallization but also influenced the elevation of the primary recrystallization starting temperature.

In the Al–Mg–Si alloy, the presence of the Mg–Si compound or Si phase cannot be ignored. Because the Al_3(Sc, Zr) particles are thermally stable with an average diameter of less than 100 nm even at temperatures of 500°C and 600°C, it is thought that they would be more effective than the Mg–Si or similar compounds in controlling the microstructures. Therefore, the thermally stable Al_3(Sc, Zr) particles are expected to contribute towards the randomization of texture and the grain refinement, without additional heat treatment process. Furthermore, these structural changes are expected to contribute to the improvement in both the formability and the strength of Al–Mg–Si alloys.

4. Conclusions

To clarify the influence of Sc and Zr on the recrystallization behavior of Al–Mg–Si alloy, the alloy with a small amount of Sc and Zr was prepared. Then, it was examined for the presence of second phase particles and its grain growth behavior during recrystallization. From this investigation, the following aspects were clarified:

(1) The grains became finer than the non-added alloy in the case of hot-rolled samples with Sc and Zr co-addition, and two types of spherical Al_3(Sc, Zr) particles, rod-like Al_3(Sc, Zr) particles and rod-like Si particles were present. It was thought that 1) the rod-like Al_3(Sc, Zr) particles were formed during the solidification, 2) spherical Al_3(Sc, Zr) particles were precipitated during the homogenization treatment, and 3) incoherent spherical Al_3(Sc, Zr) particles were formed from rod-like particles being separated during the hot-rolling.

(2) Annealing treatment of the co-added cold-rolled alloy sample showed that it consisted of elongated grains up to 500°C, and they became equiaxed at 600°C. Meanwhile, the non-added cold-rolled samples were also equiaxed at 400°C, and grains having recrystallized texture components occupied most of the sample.

(3) After the comparison of driving forces of primary recrystallization by stored strain energy owing to cold rolling and that of grain growth by recrystallized grain size as well as Zener force by Al_3(Sc, Zr) particles, Al_3(Sc, Zr) particles were found to act as the resistant to the grain growth after the primary recrystallization.

(4) To clarify the recrystallization grain growth process from 300°C to 450°C, an *in-situ* heating SEM/EBSD analysis was carried out. The results showed that the recrystallization starting temperature was increased in the co-added alloy, and the grain growth of primary recrystallization was inhibited. It also became clear that the primary recrystallization was nearly finished at 300°C in the non-added alloy, and the rolling and recrystallization texture components grew preferentially.

(5) The texture and the grain size of Al–Mg–Si alloys can be randomized and refined by the introduction of Al_3(Sc, Zr) particles, without a special thermo-mechanical treatment. It was found that Al_3(Sc, Zr) particles are effective for improving the material properties by structural control.

Acknowledgments

We would like to express their hearty thanks to Mr. Y. Nishihata and T. Yokote for their help in the experimental work. We are also thankful to Kobe Steel, Ltd., for making Al–Mg–Si–Sc–Zr alloys used in this study. The present study was financially supported by The Japan Aluminium Association, The Light Metal Educational Foundation, Inc. and JSPS KAKENHI Grant Number 16H04502.

REFERENCES

1) T. Sakurai: Kobe Steel Engineering Reports **57** (2007) 45–50.
2) K. Seto: JIDOUSHA NO KEIRYOUKA TECHNOLOGY, (NTS Inc., 2014) pp. 23–30.
3) J. Røyset and N. Ryum: Int. Mater. Rev. **50** (2005) 19–44.
4) S. Fujikawa: J. JILM **49** (1999) 128–144.
5) S. Iwamura and Y. Miura: J. JILM **56** (2006) 100–104.
6) A. Tolley, V. Radmilovic and U. Dahmen: Scr. Mater. **52** (2005) 621–625.
7) C.B. Fuller, J.L. Murray and D.N. Seidman: Acta Mater. **53** (2005) 5401–5413.
8) V. Radmilovic, A. Tolley, E.A. Marquis, M.D. Rossell, Z. Lee and U. Dahmen: Scr. Mater. **58** (2008) 529–532.
9) B. Forbord, H. Hallem, J. Røyset and K. Marthinsen: Mater. Sci. Eng. A **475** (2008) 241–248.
10) K. Ikeda, Y. Miyata, T. Yoshihara, N. Takata and H. Nakashima: J. JILM **64** (2014) 353–360.
11) S. Iwamura and Y. Miura: Acta Mater. **52** (2004) 591–600.
12) A.F. Norman, P.B. Prangnell and R.S. McEwen: Acta Mater. **46** (1998) 5715–5732.
13) C.B. Fuller, A.R. Krause, D.C. Dunand and D.N. Seidman: Mater. Sci. Eng. A **338** (2002) 8–16.
14) K. Ikeda, R. Akiyoshi, T. Takashita, M. Mitsuhara, S. Hata, H. Nakashima, K. Yamada and K. Kaneko: Proc. of 13th International Conference on Aluminum Alloys (ICAA13), (2012) pp. 1181–1185.
15) M.J. Jones and F.J. Humphreys: Acta Mater. **51** (2003) 2149–2159.
16) W.T. Read and W. Shockley: Phys. Rev. **78** (1950) 275–289.
17) W.T. Read: *Dislocation in Crystals*, (McGraw Hill, 1953).
18) F.J. Humphreys and M. Hatherly: *Recrystallization and Related Annealing Phenomena* Second Edition, (Elsevier, 2004).
19) E. Nes, N. Ryum and O. Hunderi: Acta Metall. **33** (1985) 11–22.